

<https://doi.org/10.1038/s43247-024-01564-8>

# Pathways and timescales of Southern Ocean hydrothermal iron and manganese transport



Antony J. Birchill<sup>1,2,6</sup>  , Chelsey A. Baker<sup>3,6</sup>  , Neil J. Wyatt<sup>2,4</sup>, Katsiaryna Pabortsava<sup>3</sup> ,  
Hugh J. Venables<sup>5</sup>, C. Mark Moore<sup>4</sup>, Isobel Turnbull<sup>2</sup>, Angela Milne<sup>2</sup> , Simon J. Ussher<sup>2</sup>, Sophy Oliver<sup>3</sup> &  
Adrian P. Martin<sup>3</sup>

Scarcity of iron and manganese limits the efficiency of the biological carbon pump over large areas of the Southern Ocean. The importance of hydrothermal vents as a source of these micronutrients to the euphotic zone of the Southern Ocean is debated. Here we present full depth profiles of dissolved and total dissolvable trace metals in the remote eastern Pacific sector of the Southern Ocean (55–60° S, 89.1° W), providing evidence of enrichment of iron and manganese at depths of 2000–4000 m. These enhanced micronutrient concentrations were co-located with <sup>3</sup>He enrichment, an indicator of hydrothermal fluid originating from ocean ridges. Modelled water trajectories revealed the understudied South East Pacific Rise and the Pacific Antarctic Ridge as likely source regions. Additionally, the trajectories demonstrate pathways for these Southern Ocean hydrothermal ridge-derived trace metals to reach the Southern Ocean surface mixed layer within two decades, potentially supporting a regular supply of micronutrients to fuel Southern Ocean primary production.

Despite being the largest high-nutrient low-chlorophyll region<sup>1,2</sup>, the Southern Ocean (SO) is a globally important organic carbon sink. The interplay between circulation and remineralisation dynamics set the rate of carbon uptake by the biological carbon pump<sup>3</sup> with 10% of global biological carbon export occurring in the region<sup>4</sup>. Iron (Fe) is an essential but often scarce micronutrient that can limit primary production and the efficiency of the biological carbon pump in the SO<sup>5,6</sup>. Other elements can potentially be (co-)limiting alongside Fe in the SO<sup>7</sup>, with recent evidence for manganese (Mn) (co-)limitation in particular<sup>2,8–10</sup>.

As non-conservative elements with residence times on the order of decades in the deep ocean<sup>11</sup>, the distributions of dissolved Fe and Mn (dFe, dMn; <0.2 μm) in seawater are spatially coupled to sources. The main external sources of Fe and Mn to the ocean are margin sediments, atmospheric dust, and hydrothermal venting<sup>5,12</sup>. Input from margin sediments enhances primary production downstream of islands in the SO<sup>13,14</sup>, and sustains ecosystems in Antarctic shelf regions<sup>12,15</sup>, where melting glacial ice can be an additional source of Fe and Mn<sup>16,17</sup>. Marine aerosol Fe concentrations can vary by >3 orders of magnitude, causing sporadic and seasonal changes to the widespread deposition of Fe to the surface ocean<sup>18</sup>. However, according to both observations and models, the remote southern

hemisphere oceanic gyres and polar regions have some of the lowest Fe aerosol deposition fluxes in the world (<0.01 g Fe m<sup>-2</sup> yr<sup>-1</sup>)<sup>19</sup>.

Both Fe and Mn are concentrated in hydrothermal fluids, often enriched by a factor of >10<sup>6</sup> relative to background seawater<sup>20</sup>. Early studies suggested that Fe and Mn entering the ocean from hydrothermal vents were precipitated or scavenged and sedimented close to vent sites<sup>12,21</sup>, with precipitation reported to occur before the plume reaches neutral buoyancy<sup>22</sup>. However, it is now known that a small fraction of the dFe supplied from hydrothermal vents is sufficiently stabilised against precipitation to be transported in the ocean interior<sup>23–25</sup>. Hydrothermal venting is estimated to supply 4 ± 1 Gmoles dFe yr<sup>-1</sup> to the wider deep ocean away from the proximal vent sites<sup>23,26</sup>, representing a continuous Fe input in contrast to short-term variations observed in other Fe sources, such as atmospheric deposition<sup>26</sup>. Similarly, observed increases in deep ocean dMn concentrations have been attributed to hydrothermal activity<sup>16</sup>, and incorporating hydrothermal dMn inputs increases the accuracy of modelled oceanic dMn distributions<sup>12</sup>. Our understanding of the hydrothermal plume processes responsible for the physico-chemical stabilisation of Fe is developing, though not yet comprehensive. Within hydrothermal plumes, dFe has been shown to form inorganic nanoparticles<sup>27,28</sup>, larger inorganic colloids<sup>29</sup>, and

<sup>1</sup>Chief Scientist's Group, Environment Agency, Romsey District Office, Romsey, UK. <sup>2</sup>School of Geography, Earth and Environmental Sciences, Plymouth University, Devon, UK. <sup>3</sup>National Oceanography Centre, Southampton, UK. <sup>4</sup>School of Ocean and Earth Sciences, University of Southampton, Waterfront Campus, Southampton, UK. <sup>5</sup>Polar Oceans Team, British Antarctic Survey, Cambridge, UK. <sup>6</sup>These authors contributed equally: Antony J. Birchill, Chelsey A. Baker.

 e-mail: [antony.birchill@environment-agency.gov.uk](mailto:antony.birchill@environment-agency.gov.uk); [chelsey.baker@noc.ac.uk](mailto:chelsey.baker@noc.ac.uk)

organic complexes<sup>30,31</sup>. The co-location of carbon with Fe in plume particles suggests that organic carbon may alter the chemical behaviour of Fe oxyhydroxides<sup>29</sup> and create localised regions of Fe(II) enrichment<sup>31</sup>.

Due to the inhibition of vertical mixing in the ocean interior by density stratification, hydrothermal plumes tend to travel predominantly along isopycnals<sup>32,33</sup>. Westerly winds drive the Antarctic Circumpolar Current to create a northward surface flow (Ekman Transport), causing isopycnals to shoal in the SO<sup>34</sup>. Consequently, upwelling deep waters in the SO may provide a pathway for hydrothermal trace metals to be mixed into the SO euphotic zone<sup>21,35</sup>. Inputs of hydrothermal dFe from shallow (<500 m) and deep (>2000 m) vents have been linked to regional phytoplankton blooms within<sup>36,37</sup> and outside of the SO<sup>38</sup>. The potential for hydrothermal dFe to sustain primary production in the SO has been evaluated in models<sup>39,40</sup>, but consensus on the significance of this source of Fe and Mn has yet to be reached.

To sustain SO primary production, upwelling timescales must be short enough to deliver hydrothermal Fe and Mn to the euphotic zone before removal processes, such as scavenging and precipitation, deplete these metals. Assuming that some degree of physico-chemical stabilisation of dFe in neutrally buoyant plumes may allow transportation to surface waters, model results indicate that hydrothermal Fe could support ≈15–30% of export production south of the Polar Front<sup>39</sup>. However, estimates of dFe residence time in the East Pacific Rise (EPR) far-field plume at 15° S have been revised from quasi-conservative, based on comparisons with <sup>3</sup>He measurements<sup>23</sup>, to non-conservative with a residence time of 9–50 years, based on comparisons with <sup>228</sup>Ra measurements<sup>41</sup>. The 9–50 year residence time estimate is consistent with a global modelling study estimate of hydrothermal Fe residence time of 21–35 years<sup>39</sup>. Similarly, deep ocean dMn residence times are estimated at 5–40 years<sup>11</sup>.

In comparison, transit time estimates for the shoaling of Circumpolar Deep Waters, originating in the Pacific (≥30° S), to the SO mixed layer range from 17 years to a few centuries<sup>42–45</sup>. Such uncertainty surrounding hydrothermal Fe input and stabilisation processes, alongside SO ventilation rates, is reflected in Fe modelling studies. A global steady-state inverse circulation model combined with a mechanistic Fe model was used to conclude that only 3–5% of hydrothermal dFe reaches surface waters globally<sup>40</sup>. A subsequent study argued however that the

inverse modelling approach reduces the magnitude of hydrothermal Fe inputs from ridge systems located within the SO relative to a spreading rate model approach<sup>39</sup>. This ongoing debate is hindered by a lack of observational evidence of the key transport pathways. The Southeast Pacific sector of the SO has been indicated as a critical region for hydrothermal Fe and Mn input by models<sup>12,39</sup>, but is a ‘data desert’ for trace metal observations. In this study, we provide the first full-depth profiles of Fe and Mn from this SO region, which show a clear midwater hydrothermal trace metal signal. By modelling water pathways, we trace the hydrothermal signal back to specific ridge systems and evaluate whether the observed hydrothermal Fe and Mn could supply the SO mixed layer, and therefore fuel SO primary production.

## Results and discussion

### Observations of hydrothermal trace metals in the southeast Pacific sector of the Southern Ocean

Our study sampled a north–south transect along 89° W located in the Mornington Abyssal Plain in the southeast Pacific Ocean (Fig. 1A). As expected, SO surface waters were characterised by extremely low dFe (<0.2 nM, 0–30 m depth;  $0.09 \pm 0.04$  nM,  $n = 18$ ) and total dissolvable Fe (TdFe; unfiltered) concentrations (0–30 m depth;  $0.19 \pm 0.09$  nM,  $n = 13$ ; Fig. 1B, C) and excess macronutrient concentrations (nitrate + nitrite 16.6–23.6 μM, phosphate 1.0–1.6 μM; data not shown), consistent with previous upper ocean observations in this region<sup>46</sup> and wider SO biogeochemistry<sup>35</sup>.

The most striking feature of our transect was Fe enrichment in deep waters (Fig. 1B, C), with dFe concentrations of 0.48–0.96 nM occurring between 2000 and 4000 m at the northern end of our transect Fig. 1A; Table S1). Elevated TdFe concentrations (>2.5 nM with a maximum concentration of 15.4 nM), associated with reduced dFe concentrations, were also observed in benthic nepheloid layers driven by particle accumulation and benthic sediment resuspension of particulate Fe and scavenging of dFe (Figs. 1C, 2D). For comparison, particulate Fe concentrations (up to 88 nM) were observed above the seafloor at open ocean stations in the North Atlantic<sup>47</sup>.

Away from external sources, deep ocean dMn concentrations are typically very low (<0.2 nM) due to scavenging removal into the particulate phase and oxidation of Mn ions to insoluble Mn oxides<sup>16</sup>. However, like dFe,

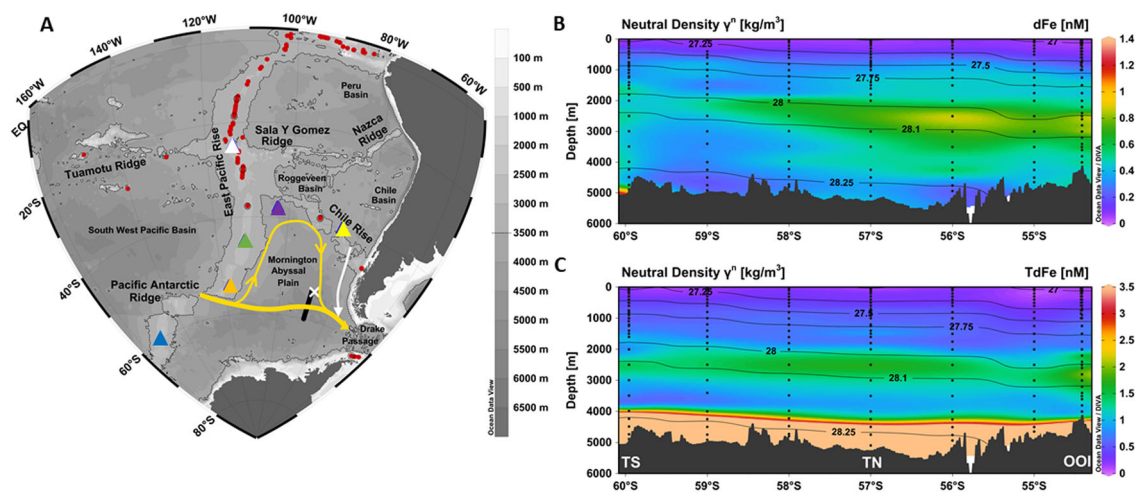
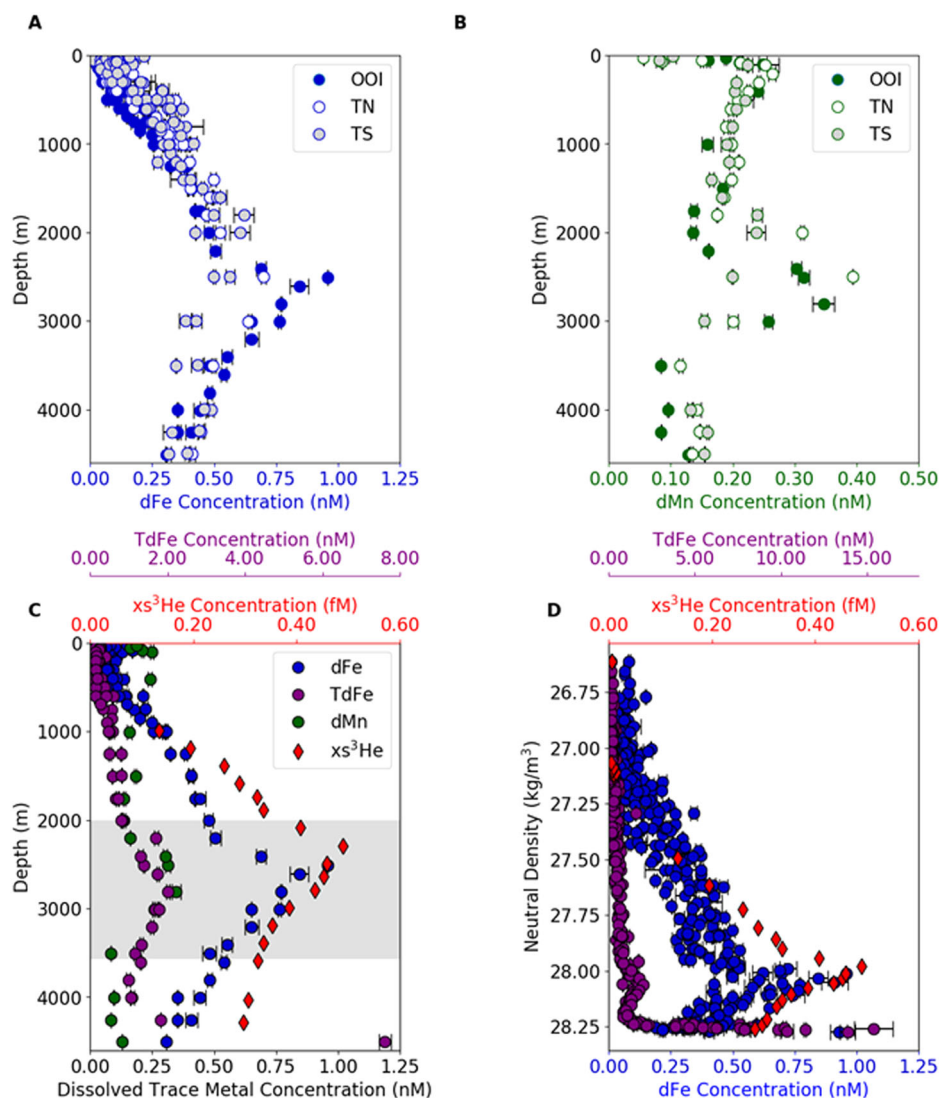


**Fig. 1 | Study region and dissolved iron and total dissolvable iron transects.**

**A** Study area in the southeast Pacific and Southern Ocean. Red dots are the location of known active vent sites<sup>82</sup>. Lack of exploration means that knowledge of active vent site locations over the region is incomplete. The yellow arrow is the approximate flow of water at 2000–4000 m depth<sup>83</sup> and white arrow is the approximate flow of Southeast Pacific Deep Slope Water<sup>54</sup>. The solid black line is the transect occupied by this study. The white cross is the sampling location of a previous <sup>3</sup>He profile<sup>49</sup> collected in 1993 ~83 km northeast (bearing of 055°) of our northernmost station. Triangles indicate the start locations for forward-tracked trajectory modelling in this study: yellow—East Chile Rise, purple—West Chile Rise, white—Easter

Microplate, green—North East Pacific Rise, orange—South East Pacific Rise (SEPR) and blue—Pacific Antarctic Ridge (PAR). **B**, **C** Section plots of dFe (<0.2 μM) and TdFe (unfiltered) concentrations along the transect with neutral density overlain. Black dots mark sampling depths. Note that concentrations in (**B**) and (**C**) are on different scales and that TdFe concentrations were typically >2.5 nM near the seafloor. The maximum concentration measured was  $15.39 \pm 1.12$  nM. OOI is the sampling location coinciding with the Ocean Observatories Initiative sustained observatory location, 54.08° S 89.67° W, <https://oceanobservatories.org/array/global-southern-ocean-array>. Stations OOI, TN, and TS (**C**) are the locations of trace metal depth profiles displayed in Fig. 2.

**Fig. 2 | Depth profiles of iron, manganese and excess helium.** **A** Depth profiles of dFe at stations OOI, TN and TS. **B** Depth profiles of dMn at stations OOI, TN and TS. **C** Depth profiles of dissolved trace metals (dFe and dMn) and TdFe at our northernmost station OOI (combined Fe data from four site visits) and nearby historic  $xs^3He$  (see Fig. 1A; white cross). **D** All dFe and TdFe data from the transect and nearby historic  $xs^3He$  plotted against neutral density. Error bars for dFe and TdFe are the range of duplicate analyses and for dMn the standard deviation of triplicate analysis.



basin-scale transport in vent plumes has been observed e.g. westward transport of dMn from the EPR (10–17° S) occurs in the low latitude Pacific Ocean<sup>23</sup>. Along our transect we present, elevated dMn concentrations (up to 0.39 nM, Table S1) occurred coincidentally with the enriched dFe signal (Fig. 2A–C), compared to a background dMn concentration (~0.2 nM) immediately above and below the mid-depth enrichment (Fig. 2B, C). The Fe and Mn enrichment we observed was centred on a neutral density surface of  $\Upsilon_n = 28.0\text{--}28.1 \text{ kg m}^{-3}$  (Fig. 2D), within Circumpolar Deep Water (Fig. S1). In the southwest Pacific (170° W), Circumpolar Deep Water has background dMn concentrations of ~0.1–0.2 nM<sup>48</sup> away from hydrothermal and sediment inputs. The  $\Upsilon_n = 28.0\text{--}28.1 \text{ kg m}^{-3}$  density surface shoals by ~880 m towards the south of the transect as part of the wider Ekman driven upwelling occurring in the SO. The influence of this wind-driven upwelling is shown clearly in the maximum dFe concentrations, which tracked the isopycnals along the depth section (Fig. 1) and in the dMn profiles from stations OOI, TN and TS (Figs. 1B, C and 2A, B; Table S1).

Mantle helium (He), which is enriched in primordial  $^3He$ , is also released into the ocean at mid-ocean ridges. A ratio of  $^3He/^4He$  in excess of atmospheric values (hereafter  $xs^3He$ ) in deep ocean waters is a widely used tracer of hydrothermal inputs<sup>49</sup>, though the basin-scale hydrothermal Fe supply from SO vents may not be well predicted by the spatial distribution of  $^3He$  inputs, likely because of inter-vent  $Fe:^3He$  ratio variability<sup>39</sup>. Nevertheless, at a single location, the coincident enrichment of  $^3He$ , Fe and Mn in deep ocean waters is indicative of hydrothermal input of these elements.

Helium isotope observations, previously sampled near station OOI (Fig. 1), revealed the presence of  $xs^3He$  at the depths and neutral density of our observations of trace metal enrichment (Fig. 2C, D). Although the helium dataset was collected 26 years and 83 km away from our trace metal observations, the comparable distribution of dFe, TdFe and  $xs^3He$  with neutral density (Fig. 2D) provides confidence that we observed a consistent oceanographic signal in both datasets. However, we cannot account for any temporal variability of end-member metal and helium concentrations during the 26-year gap between trace metal and helium sample collection<sup>50</sup>. The Fe concentration maximum at the northern end of our study site was slightly deeper (215 m) than the mantle  $xs^3He$  maximum. A similar offset in the distribution has been observed further north in the far-field plume of the EPR (20–26° S) and has been attributed to the reversible scavenging of dFe onto sinking particles, which deepens the metal concentration maximum<sup>51</sup>. The offset we observed may also be due to temporal variability of end-member metal and helium concentrations, the influence of multiple vent sites with varying  $Fe:^3He$  ratios, and/or reversible scavenging combined with layering of fine particulate material with irregular element distribution within plumes<sup>52</sup>.

The balance between the release of dFe from remineralising organic matter and removal of dFe from solution via scavenging processes leads to an accumulation of dFe in Pacific Mode and Intermediate Waters<sup>53</sup>. We show that the signal we observed is decoupled from the mineralization of biogenic particles by plotting dFe against apparent oxygen utilisation (Fig. S2). In waters below the mixed layer, there is a positive linear relationship between



dFe and apparent oxygen utilisation indicating that remineralisation of sinking organic matter exerts an important control on dFe concentrations, consistent with previous investigations of Pacific mode and intermediate waters<sup>53</sup>. However, the enrichment of dFe we observed in deeper waters clearly deviates from the linear dFe- apparent oxygen utilisation trend, indicating an additional deep water dFe source such as long-range transport of hydrothermal dFe<sup>24</sup>.

**Identifying the source region of the observed hydrothermal signal**

The bathymetry of the southeast Pacific Ocean has several mid-ocean ridge systems (Fig. 1A), the most prominent being the EPR which is aligned meridionally at ~115° W at depths of around 2500 m. The southern extension of the EPR, the Pacific Antarctic Ridge (PAR), is aligned zonally (~55–65° S). The Chile Rise (CR; ~40–45° S) bounds the North of the Mornington Abyssal Plain (our study region) between the EPR and the coast

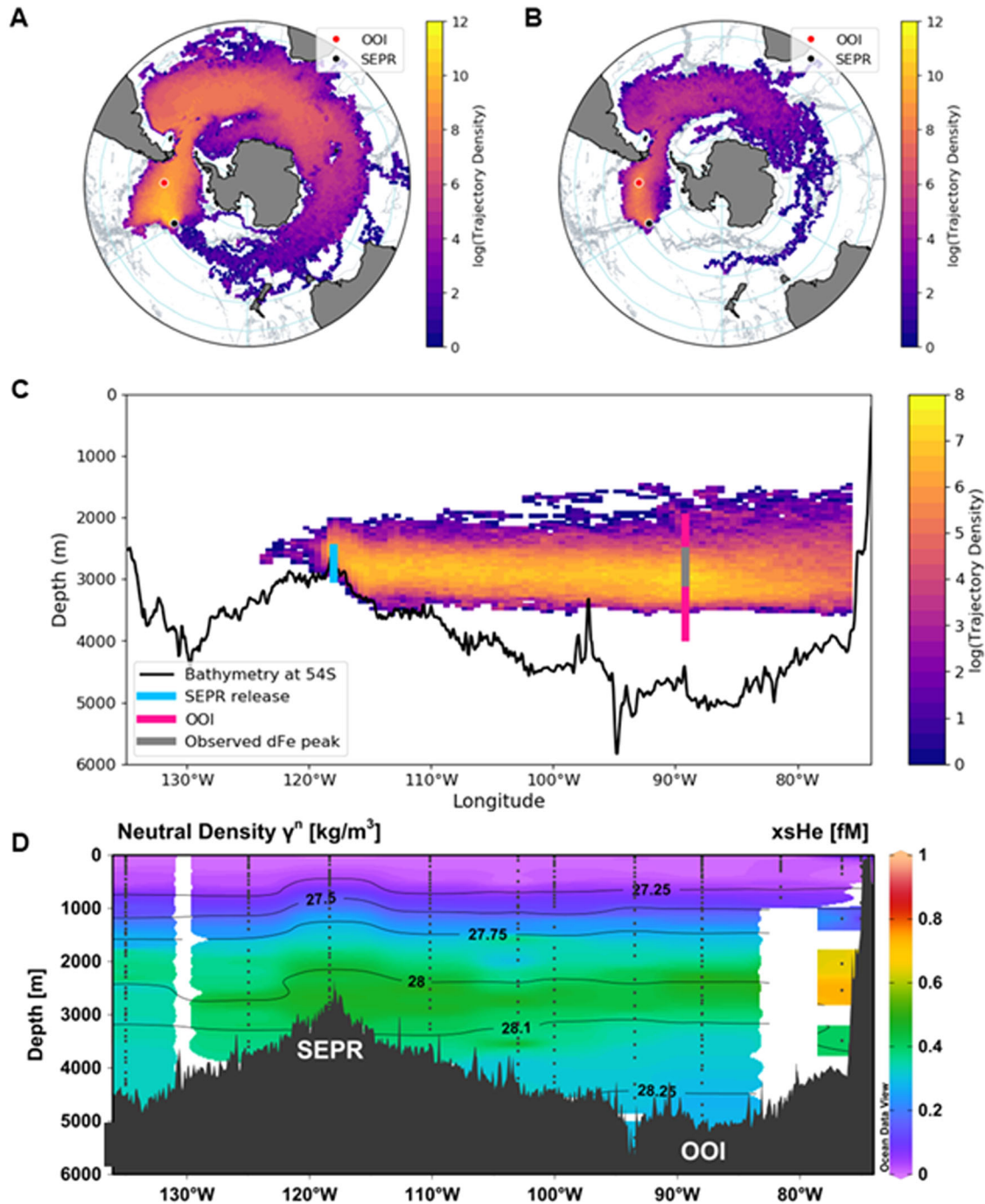


**Fig. 3 | Forward-tracking simulations from the Southeast Pacific Rise and coincident xs<sup>3</sup>He anomaly.** Trajectories of the forward-tracking simulations from the SEPR (A–C) and coincident xs<sup>3</sup>He anomaly (D). Trajectories were released between the ridge and 500 m above to mimic a neutrally buoyant hydrothermal plume. **A** Trajectory density, which indicates the number of instances of trajectories passing into a grid cell (log scale), of all SEPR trajectories. **B** Trajectory density map of SEPR trajectories that pass within a 0.5° area around the OOI station (red marker). **C** Depth section of trajectory density for the SEPR trajectories that pass within a 0.5°

area of the OOI station (location indicated by pink line). Additionally, the grey line superimposed on the pink line highlights the depth range where dFe concentrations were >0.75 nM (Fig. 2). The cyan line marks the trajectory seeding depth which mimics a neutrally buoyant plume. Bathymetry along 54° S (to match station OOI) is shown. Note the colour bar scale is different for (C) compared to (A, B). **D** An east-west transect of excess Helium (xs<sup>3</sup>He) at 54° S as an indicator of hydrothermal influence from the Jenkins et al. dataset<sup>19</sup>.

of Chile. The OOI site is a little south of the confluence of the easterly flowing Antarctic Circumpolar Current and the eastern boundary current. The latter flows within ~1500 km of the coast of South America between 1500 and 3500 m, this Southeast Pacific Deep Slope Water<sup>54</sup> represents the main route for mid-depth flow in the South Pacific to enter the SO<sup>54–56</sup>. Volcanic activity at multiple sites along ridge systems (Fig. 1A), alongside complex interior circulation, results in widespread xs<sup>3</sup>He in intermediate and deep waters (~1000–4000 m) in the South Pacific Ocean<sup>45</sup>. A previous meridional transect along 88° W shows the southward extension of xs<sup>3</sup>He towards our study area (Fig. S3A), which could indicate plumes originating from ridges to the north e.g. the Sala Y Gomez Ridge and CR (Fig. 1A). Similarly, a zonal transect along 54° S shows an eastward extension of xs<sup>3</sup>He from the South EPR (SEPR) that intersects the OOI station (Fig. 3D; Fig. S3B). Because the xs<sup>3</sup>He observations do not allow us to discern a clear source region, we undertook trajectory tracking simulations to provide an independent estimate for the origin of the hydrothermal signal.

To trace trajectories from potential sources, a series of model release sites were first selected. Along the poorly explored southern ridge systems, bathymetry along with xs<sup>3</sup>He observations and previous literature<sup>33</sup> were used to select an arc of potential release sites to the north and west of station OOI. To simulate a neutrally buoyant hydrothermal plume, trajectories were initiated within a 0.5° grid around an assumed source extending 500 m upwards in the water column above the ridge at the West Chile Rise (WCR), East Chile Rise (ECR), North EPR (NEPR), SEPR and PAR South (PARS) locations (Fig. 1; Table 1) and tracked forwards in time. A reverse simulation was also performed whereby trajectories were backtracked from within a 0.5° grid around the OOI site between 2000 and 3950 m depth, coincident with our hydrothermal Fe and Mn enrichment observations (Table 1; Fig. 2C), towards the ridge systems. The mid-ocean ridge system surrounding our study region was divided into five regions (Fig. S4; Table S4), including an additional region PAR North (PARN) which did not have a forward-tracking release site. We quantified the backwards trajectories that passed through the likely plume depths (i.e. extending up to 500 m of water column above a ridge<sup>57–59</sup>) in these regions (Tables 1 and S2). For both forward and backwards tracking, trajectories were traced for 20 years by applying a Lagrangian simulator, called ‘parcels’ (<https://oceanparcels.org/><sup>60</sup>), to the velocity components of a global ocean model (Nucleus for European Modelling of the Ocean; NEMO)<sup>61</sup> at an eddy-resolving (0.083°) horizontal resolution. Trajectories estimate the flow of water within the model ocean and do not represent concentrations of trace metals.

Trajectory estimates strongly supported a westerly source region with no influence from northerly ridge systems (Table 1). The SEPR region is identified as the most likely source for our observed signal. Forward-tracking simulations from the SEPR resulted in the greatest percentage of

trajectories (9%) crossing within a 0.5° area around OOI at a depth coincident with the observed Fe and Mn enrichment compared to other release sites (Fig. 3C; blue line). Similarly, in the backward-tracking simulations, the greatest percentage of trajectories (21%) released from OOI passed within the SEPR source region (Table 1). In an oceanographic context, these percentages can be thought of as demonstrating the strength and coherency of transport pathways within the wider ocean circulation between the source regions and OOI i.e. the greater the percentage the more dominant the pathway. The SEPR also had the shortest median transit timescales to/from OOI (10–12 years). Further west, the backward-tracking simulations indicate that 8–20% of trajectories starting at OOI intersect with the PAR ridge systems with a median transit time of 13–14 years. However, the peak in the trajectory signal propagated from the PAR regions was deeper than the observed Fe and Mn peaks at OOI, especially for PARS (Fig. S3H). Our transit time estimates from the SEPR and PAR are at the lower end of estimated hydrothermal dFe residence times of 9–50 years<sup>39,41</sup>.

The NEPR makes a minor contribution in both forward and backward trajectories over 20 years (0.3–1.3% of trajectories to/from OOI), with trajectories exhibiting longer median transit times to reach OOI (14–18 years), despite being much closer in proximity to OOI than the PARS site which made the second largest contribution (Fig. 1; Table 1). Similarly, trajectories from the CR did not intersect with the OOI site within 20 years.

Our simulations indicate minimal exchange between waters north and south of 45° S in the Mornington Abyssal Plain, likely due to the South Pacific Current, which has diverging pathways above and below 40–43° S<sup>55,62</sup>. This interpretation is supported by a model validation between the NEMO model used for the trajectory simulations and the Estimating the Circulation and Climate of the Ocean (ECCO) model state estimate<sup>63,64</sup> (Fig. S5). Both showed that the dominant currents at OOI originate from the west with weaker currents north of 45° S. Overall, the trajectory simulations indicated that the observed OOI trace metal plume originates from a ridge to the west of OOI, which is consistent with our understanding of the fast-moving Antarctic Circumpolar Current and weak currents in the northern Mornington Abyssal Plain<sup>65</sup>. Therefore, the strong xs<sup>3</sup>He signal to the north in the Mornington Abyssal Plain region (Fig. S3A) should not be interpreted as traversing southwards towards OOI. Our results indicate that the xs<sup>3</sup>He signal observed at OOI has most likely traversed eastwards from the SEPR and/or from along the PAR (Fig. 3D). The PARS/N trajectory simulations highlight a pathway for potential hydrothermal transport along the PAR, that tracks northwards up to the SEPR and then eastwards towards the OOI site (Fig. S4E, G). Thus, it is possible we observed the amalgamation of trace metal inputs from multiple vent sites along the PAR and SEPR at the OOI site and along the transect, rather than a discrete single vent signal.

**Table 1 | Summary of trajectory simulations used to identify possible hydrothermal source regions**

Experiment type	Trajectory starting point	Observed signal	Ridge depth (m)	Trajectory seeding depth range (m)	Proportion of trajectories that passed near observed signal (%)	Median first passage time (years from start)
Forward	ECR	OOI	3900	3400–3900	0	>20
Forward	WCR	OOI	3900	3400–3900	0	>20
Forward	SEPR	OOI	3000	2500–3000	9.5	9.8
Forward	NEPR	OOI	3200	2700–3200	0.3	17.9
Forward	PARS	OOI	2800	2300–2800	0.9	15.1
Experiment type	Trajectory starting point	Source region	Ridge depth (m)	Plume source depth range (m)	Proportion of trajectories that passed near potential source (%)	Median first passage time (years from start)
Backward	OOI	ECR/WCR	3900	3400–3900	0	>20
Backward	OOI	SEPR	3000	2500–3000	20.7	11.8
Backward	OOI	NEPR	3200	2700–3200	1.3	14.4
Backward	OOI	PARN	3000	2500–3000	20.3	12.7
Backward	OOI	PARS	2800	2300–2800	7.7	14.4

The proportion of trajectories that passed within a 0.5° area around the OOI site is presented relative to the number of particles that were successfully released during each simulation (Tables S2 and S3). The source regions that trajectories were tracked backwards in time towards were much larger than the area around station OOI, as they span along sections of the ridges, allowing more trajectories to pass into the source regions in the backward-tracking simulations (Tables S2, S3 and S4).

Systematic surveying for hydrothermal activity is lacking for the majority of the southern EPR and PAR systems<sup>66</sup>. However, it is expected that the ridge system is hydrothermally active as multiple lines of evidence suggest that hydrothermal venting is common. Metalliferous sediments (enriched in Fe and Mn compared to aluminium), formed by the precipitation of Fe and Mn from hydrothermal fluids, are found along these ridge systems<sup>67</sup>. Additionally, the magmatic budget hypothesis<sup>66</sup> predicts that variability in magma supply is the primary control on the large-scale hydrothermal distribution pattern along spreading ridges and is supported by a linear relationship between spreading rate and frequency of vent fields. Extrapolation of this relationship has been used to estimate a total of ≈200–300 undiscovered vent fields along the SEPR and PAR with an average distance between vent fields along the SEPR of 25–30 km<sup>66</sup>. Indeed, high-resolution optical and redox sensor measurements made along 1470 km of intermediate and fast-spreading mid-ocean ridge suggest that the frequency of vent sites is 3–6-fold higher than current observations (Fig. 1A), with a mean discharge spacing of 3–20 km<sup>68</sup>.

Similarly, evidence from observational and modelling studies exists for the long-range transport of chemical signatures from these ridge systems. For example, sections of the PAR (south of 55° S) were identified as the likely source region of a <sup>3</sup>He anomaly found on the neutral density surface  $\sigma_{\theta} = 28.2 \text{ kg m}^{-3}$ , indicative of active venting<sup>33</sup>. Modelling dFe hydrothermal vent input as a function of ridge spreading rate found good agreement with observed dFe anomalies in the abyssal SO, with some of the highest rates of hydrothermal Fe input in the Pacific sector along the PAR and SEPR<sup>30</sup>. Similarly, a global ocean modelling simulation of Mn predicted strong input from the SEPR which produced a dMn anomaly that extends to the location of our transect<sup>12</sup>.

### Could hydrothermal iron and manganese from southeast Pacific vents fuel Southern Ocean primary production?

The potential for hydrothermal Fe and Mn to fuel primary production depends on the balance between Fe and Mn residence times and the ventilation timescale of hydrothermal plume-influenced waters. A transit time of  $99 \pm 18$  years for the shoaling of deep waters to the SO surface has been estimated using a global <sup>3</sup>He mass balance model, in which <sup>3</sup>He predominantly enters into the SO via deep South Eastern Pacific waters<sup>45</sup>. Deep ocean re-exposure timescales of a few centuries have also been calculated using a low horizontal resolution (2°) global steady-state ocean circulation inverse model<sup>42</sup>. These ventilation timescales are likely incompatible with the notion that Fe and Mn from southeast Pacific vents could sustain SO productivity when compared with estimated seawater residence times for Fe and Mn. Indeed, coupling a mechanistic Fe model, where hydrothermal input is estimated from a fixed Fe:<sup>3</sup>He ratio, with an ocean inverse circulation model allows for scavenging processes to effectively trap hydrothermal Fe in the deep ocean<sup>40</sup>.

However, uncertainty around the magnitude of hydrothermal Fe input from SO ridge systems, and accounting for mesoscale processes when estimating ventilation timescales, may in fact allow for rapid transport of hydrothermal Fe and Mn to upper ocean waters. An inverse modelling approach reduces the magnitude of <sup>3</sup>He input from SO ridge systems relative to a spreading rate model approach. A spreading rate model estimates <sup>3</sup>He input as a function of ridge spreading rate, and likewise assigns an Fe:<sup>3</sup>He ratio to estimate a hydrothermal Fe flux<sup>39</sup>. Comparisons with observed dFe concentrations revealed that the inverse model approach does not replicate the magnitude of an observed SO hydrothermal dFe signal from the GEOTRACES GS01 section South of Tasmania<sup>39</sup>. A consequence of the spatial redistribution of hydrothermal Fe input away from the SO vent sites by the inverse modelling approach is a reduction in the estimated amount of hydrothermal Fe reaching the upper 250 m of the ocean by 4–5-fold relative to the spreading rate model<sup>39,40</sup>. It is also possible that previous studies may be over-estimating ventilation times due to their coarse resolution. Mesoscale (10–100 km) processes are important conduits for vertical mixing in the SO<sup>43,44</sup>. Using a Lagrangian particle tracking model transit times of 17–90 years were estimated for Circumpolar Deep Waters

(originating from 30° S between 1000 and 4000 m) to upwell to the SO mixed layer<sup>43,44</sup>. Importantly, transit time estimates decrease as model resolution becomes finer<sup>43,44</sup> with the shorter 17-year timescale estimated using a 0.1° eddy-resolving model. This highlights that accounting for mesoscale eddies is important for estimates of timescales for SO upwelling<sup>44</sup>.

To investigate the potential fate of the observed dFe and dMn signals, we continued to forward-track trajectories that passed through our cruise transect at depths of the observed trace metal peak (2000–4000 m; Fig. 4). We thus estimated the proportion of trajectories which shoal to depths coincident with SO winter mixed layer depths, the key seasonal supply mechanism of micronutrients to SO surface waters<sup>35</sup>. Eighty-three percent of the trajectories passing through the cruise transect between 2000 and 4000 m continued east through the Drake Passage and then flowed northward away from the polar front (~60° S) into deep water masses (Fig. 4A; median depth 2087 m), and so are unlikely to supply hydrothermal Fe and Mn to the SO mixed layer. However, trajectories which pass through the Drake Passage and traverse pathways south of 60° S (17%) tended to shoal in the water column by the end of the 20-year simulation (median depth 1043 m). Of the 17% of trajectories that passed south of 60° S, 10% (i.e., 1.7% of total trajectories) reached depths shallower than 600 m, a proxy for the typical winter maximum mixed layer depth in deep mixing regions of the SO<sup>69</sup>, while 31% (i.e. 5.3% of total) reached shallower than 1000 m, the maximum observed winter mixed layer depth<sup>69</sup>.

Our simulated trajectories thus indicate pathways from the observed deep southeast Pacific sector of the SO to the SO mixed layer within 20 years. Furthermore, the number of trajectories south of 60° S reaching winter mixing depths is likely to continue to increase beyond the temporal limit of our simulations (20 years). As discussed above, resolving mesoscale features in high-resolution models, as in our study (0.083° horizontal resolution), results in SO ventilation timescale estimates (within 20 years) that allow for hydrothermal Fe and Mn from SO vents to reach SO mixed layer depths within estimated Fe and Mn residence times (5–50 years)<sup>41</sup>. Moreover, the effects of submesoscale mixing and dispersion, which will influence the transport and shoaling rates of dissolved constituents, are not resolved in the physical model driving our trajectory calculations but could further shorten ventilation timescales<sup>70</sup>. Trajectory modelling offers an alternate approach to identifying hydrothermal source regions and ventilation pathways and timescales, which may be more tractable for localised studies. It remains challenging to isolate what drives the differences between Fe supply from different modelling approaches<sup>39,40</sup> and ventilation timescales from high-resolution studies (<20 years)<sup>43,44</sup>, compared to coarse resolution or global inventory studies (~100 years)<sup>42,45</sup> discussed above, as several factors change in tandem. The significance of transport pathways to the mixed layer must ultimately depend on the residence times of hydrothermal Fe and Mn being comparable or longer than the ventilation timescales we predict, as well as the consistency and stability of hydrothermal Fe and Mn inputs, both of which remain poorly constrained.

### Conclusion

We identify potential pathways for Fe and Mn from SO hydrothermal vents to reach the SO mixed layer. Enhanced Fe and Mn concentrations were observed between 2000 and 4000 m depths within the southeast Pacific sector of the SO. The observed trace metal enrichment most likely originated from the SEPR (south of 30° S). An origin further westward, such as from the PAR, was also possible. We further identified pathways for rapid (<20 years) transport of water parcels enriched in hydrothermal Fe and Mn, from vents located within the understudied Pacific sector of the SO, to SO winter mixed layer depths. Consensus on the role of deep ocean hydrothermal trace metal inputs in fuelling upper ocean primary production has not yet been reached, with modelling studies disagreeing on the importance of SO vent systems for supplying hydrothermal Fe supply to the wider SO euphotic zone<sup>39,40</sup>. However, we conclude that due to the vigorous action of the Antarctic Circumpolar Current, Pacific sector SO hydrothermal inputs provide the potential for sustained input of Fe and Mn to the euphotic zone south of the Antarctic Polar Front and far downstream of the deep ocean vent sites, potentially fuelling



productivity in remote areas of the SO. Given the existence of ridge systems throughout the SO, it is likely that other similar pathways exist that rapidly transport Fe and Mn from vent sites to the SO euphotic zone.

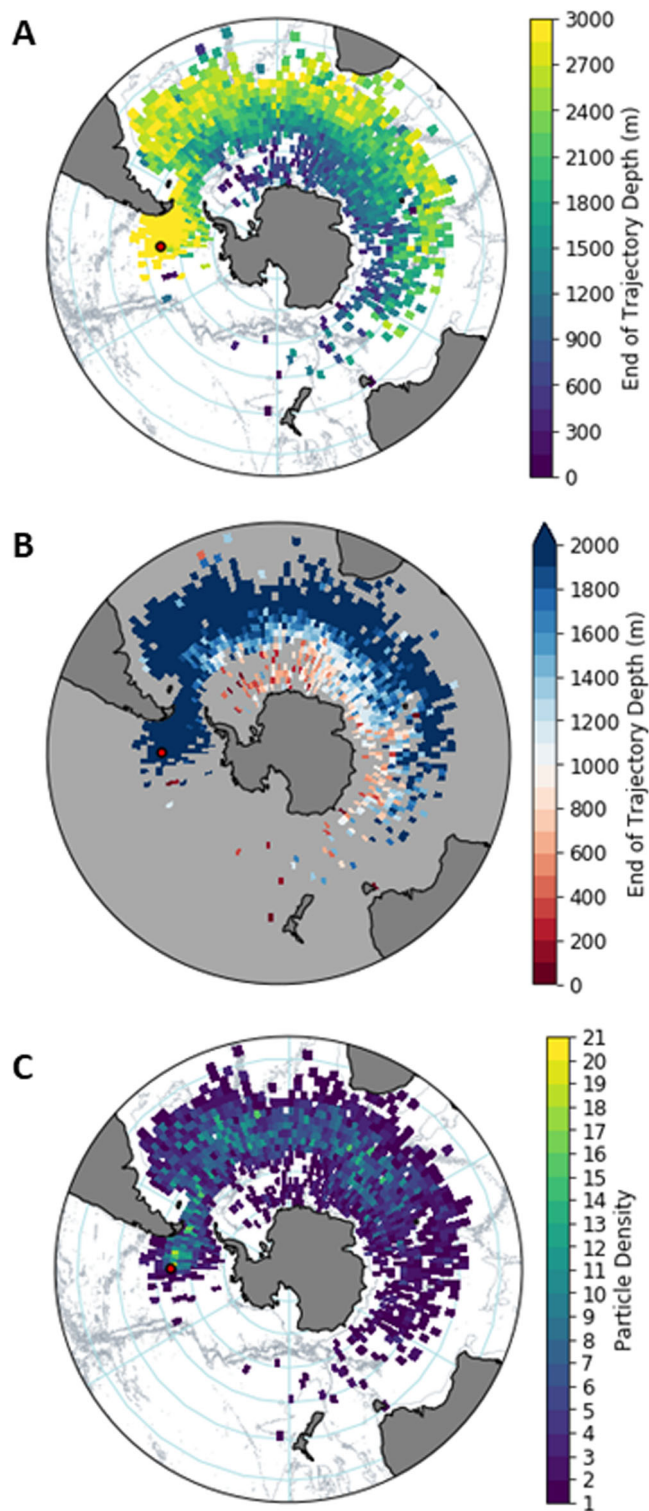


**Fig. 4 | Trajectory locations at the end of the 20 years simulation.** Indication of trajectory locations at the end of the 20-year simulation from the source regions. **A** Trajectory depth and location at 20 years and **B** the depths presented as above (red) and below (blue) the absolute maximum winter mixed layer depth in the SO (1000 m). **C** Trajectory density at 20 years. OOI is shown by the red marker. Note that only trajectories that passed within the cruise transect (OOI to 60° S) and the observed hydrothermal signal depth range (2000–4000 m) are shown.

## Methods

### Trace metal and macronutrient methods

Sampling was conducted during December 2019 and January 2020 on board the RRS Discovery along a transect in the eastern Pacific sector of the SO (Fig. 1). All trace metal samples were collected following GEOTRACES protocols<sup>71</sup>.

Briefly, dFe (0.2  $\mu\text{m}$  filtered) and TdFe (unfiltered) were analysed using flow injection with chemiluminescence detection, after spiking with hydrogen peroxide<sup>72</sup>, in a clean laboratory at the University of Plymouth. The mean limit of detection was  $0.012 \pm 0.009$  nM and the limit of quantification was  $0.038 \pm 0.026$  nM ( $n = 54$ ). Additional seawater samples collected in >1 L volumes, and acidified for >6 months, were used as in-house quality control materials as a measure of precision and were analysed every ten samples. Four in-house quality control materials were analysed; #1  $0.17 \pm 0.01$  nM ( $n = 45$ ), #2  $0.22 \pm 0.04$  nM ( $n = 54$ ), #3  $0.26 \pm 0.03$  nM ( $n = 124$ ) and #4  $0.19 \pm 0.03$  nM ( $n = 70$ ). GEOTRACES GSP and SAFe D1 and S consensus values were analysed to determine accuracy, consensus values are (GSP  $0.16 \pm 0.05$  nM, D1  $0.65 \pm 0.04$  nM, S  $0.10 \pm 0.01$  nM), which compared well to values determined (GSP  $0.20 \pm 0.020$  nM, D1  $0.66 \pm 0.066$  nM, S  $0.10 \pm 0.01$  nM). The authors have previously published bottom-up and top-down combined analytical uncertainty estimates ( $u_c$  5–10% ( $k = 1$ )) for this technique<sup>73,74</sup>.

A subset of samples from the northern, middle, and southern stations were chosen for further trace metal analysis. dMn (0.2  $\mu\text{m}$  filtered) concentration was determined using a standard addition method with off-line pre-concentration and subsequent high-resolution ICP-MS<sup>29</sup> at the National Oceanography Centre, Southampton, UK. The mean limit of detection was  $0.011 \pm 0.004$  nM ( $n = 3$ ). Consensus values for SAFe S ( $0.812 \pm 0.062$  nM) and D2 ( $0.360 \pm 0.051$  nM) reference material compared well with our measured values ( $0.769 \pm 0.059$  nM and  $0.372 \pm 0.030$  nM, respectively).

### Inorganic nutrient analysis

Seawater samples were analysed for nitrate (determined as nitrate + nitrite;  $\text{NO}_3^- + \text{NO}_2^-$ ), silicate ( $\text{SiO}_4^{4-}$ ), nitrite ( $\text{NO}_2^-$ ) and phosphate ( $\text{PO}_4^{3-}$ ). Samples were drawn from Niskin bottles into rinsed 15 mL centrifuge tubes. Colorimetric analysis was undertaken within 24 h of the samples being taken and performed using SEAL QuAatro 39 segmented flow autoanalyser<sup>75</sup>. Two sets of certified reference materials (CRM Lots CJ and CB, KANSO, Japan) were determined at a start and the end of each sample run to ensure accuracy. Depending on an analysis run, the detection limits for each parameter ranged as follows: 0.02–0.2  $\mu\text{M}$  for nitrate + nitrite, 0.02–0.15  $\mu\text{M}$  for silicate, 0.01–0.033  $\mu\text{M}$  for nitrite, and 0.002–0.019  $\mu\text{M}$  for phosphate.

### Temperature and salinity calibration

Trace metal clean samples were taken with a titanium frame Conductivity Temperature Depth (CTD) fitted with 10 L Niskin bottles and an SBE 9 plus underway unit. Conductivity (and calculated salinity) data were calibrated against samples taken from each cast and run on an Autosol 8400B salinometer. The salinity was accurate to within  $\pm 0.004$ . There was no SBE35 thermometer fitted on the titanium frame but comparison with co-located calibrated stainless steel casts showed good agreement and data is accurate to better than  $\pm 0.005$  °C.

### Excess helium calculations

$^3\text{He}$  is a primordial substance trapped in the mantle during planetary formation. Ratios of  $^3\text{He}/^4\text{He}$  in excess of atmospheric values indicate a contribution from the mantle, therefore  $^3\text{He}$  can be used to identify ocean waters that have been influenced by hydrothermal activity. Excess  $^3\text{He}$  is the approximate measure of non-atmospheric  $^3\text{He}$  over saturation, we followed the approach outlined in ref. 23 (Eq. 1):

$$^3\text{He}_{\text{xs}} = (\delta^3\text{He} - \delta^3\text{He}) / 100 \times \text{C}[\text{He}] \times 1.384 \times 10^{-6} \quad (1)$$

where  $\delta^3\text{He} = 100 \times (\text{Rx}/\text{Ra} - 1) \times 100\%$ , Rx and Ra are the  $^3\text{He}/^4\text{He}$  ratios of the sample and air ( $1.384 \times 10^{-6}$ ), respectively.  $\delta^{*3}\text{He}$  is the helium isotope ratio anomaly in solubility equilibrium with the atmosphere.

### Trajectory modelling

To identify the potential source of the observed hydrothermal Fe and Mn signal we focus on regions along the CR, EPR (NEPR and SEPR) and PAR (PARN and PARS), with regions of suspected hydrothermal activity shown in Fig. 1A (triangles).

Trajectories were used to identify the region(s) that were most likely to be the source of the deep water hydrothermal iron signal. Trajectories were tracked forwards from possible vent sites which may act as a source, and backwards from the OOI sustained observatory site, where enrichments in midwater micronutrient concentrations were observed. The velocity components used to calculate trajectories do not represent submesoscale mixing or dispersion processes<sup>60</sup>, which may affect the pathway of dissolved constituents in the ocean.

We estimated 20-year trajectories using ‘parcels’ (version 2.2.0; <https://oceanparcels.org/><sup>60</sup>). Parcels were applied to the NEMO eddy-resolving general circulation model (ORCA0083-N06<sup>61</sup>). Model output at 1/12° horizontal resolution from 1992 to 2011 was used as a 20-year climatology of the hydrodynamic flow field. NEMO was coupled to a sea-ice model (LIM2<sup>76</sup>) and was forced with historical atmospheric reanalysis (Drakkar Forcing Set 5.2<sup>77</sup>). The simulations were carried out using 3D Runge-Kutta fourth order (RK4) timestep integration as the advection scheme with a timestep of 1 day to estimate the trajectories<sup>78</sup>. The trajectory position was exported every 5 days.

Applying ‘parcels’ to velocity components on a C grid whilst using an RK4 advection scheme, with a Lagrangian timestep of 1 day, can lead to trajectories ‘overshooting’ the ocean grid cells into bathymetry. To reduce the occurrences of particles travelling out of bounds we added a criterion that returned such trajectories to 10 m above the seafloor<sup>79</sup>. This criterion was applied to 4.7% of the total timesteps in the backward-tracked trajectories and for an average of 22.9% of timesteps for the forward-tracked trajectories, due to the trajectory start locations being in close proximity to seafloor topography, i.e. vent sites along ocean ridges.

### Forward-tracking trajectories

Six potential source regions were identified (Fig. 1A, triangles) and referred to as the ECR, WCR, Easter Microplate (EM), NEPR, SEPR and PAR (Table S2). Trajectories were initialised over a 0.5° grid around each potential source location at 100 m intervals between 2000 and 4000 m. Two thousand trajectories were initiated per depth. In regions of bathymetry shallower than 4000 m, fewer trajectories were tracked. All calculations were normalised to the number of successfully tracked trajectories (Table S2) that were within a plume. We define the plume by the deepest depth of successful trajectories initialisation within each 0.5° release area, to mimic the deepest possible vent depth, up to 500 m shallower in the water column. Trajectories that crossed within a 0.5° area around the OOI site were isolated to estimate the dilution percentage of trajectories from the source regions (trajectory start locations) to OOI (Table S3). The EM had no trajectories passing near the OOI site and was not included in the analysis (Table S2).

### Backward-tracking Trajectories

To complement the forward tracking we initiated trajectories throughout the water column at OOI to coincide with the depths at which the dFe and dMn signal was observed. Trajectories were initialised over a 0.5° grid around the OOI sustained observatory site every 50 m between 2000 and 4000 m. One thousand trajectories were released per depth and tracked backwards in time for 20 years (2011–1992; Table S2).

We defined five potential hydrothermal signal source regions along the PAR, EPR and CR to further evaluate where the iron signal was most likely to originate from—ECR and WCR as CR, NEPR, SEPR, PARN, and PARS (Table S4). Trajectories were only classed as originating from that source

region if they entered at depths within a range of 500 m above the deepest possible vent height within each release area to mimic a plume<sup>80,81</sup>. For PARN, which had no specific vent release site for the forward-tracking simulation, a vent depth of 2500 m was chosen by examining the depths of the topography within the PARN area as a histogram to identify the ridge depths. The fraction of trajectories passing into each source region is presented as the dilution percentage (Table 1).

### Data availability

Lagrangian trajectories from the tracking using parcels are available at Zenodo (<https://doi.org/10.5281/zenodo.8153763>). The NEMO model velocity components used to force parcels can be found on JASMIN (<https://www.ceda.ac.uk/services/jasmin/>). The micronutrient data have been submitted to the British Oceanographic Data Centre (<https://doi.org/10.5285/0c7760cc-98fb-5861-e063-6c86abc0a998>). The macronutrient data are available from the British Oceanographic Data Centre (Series Document—BODC Document 2121989).

Received: 15 August 2023; Accepted: 15 July 2024;

Published online: 02 August 2024

### References

- Boyd, P. W., Arrigo, K. R., Strzepek, R. & van Dijken, G. L. Mapping phytoplankton iron utilization: insights into Southern Ocean supply mechanisms. *J. Geophys. Res. Oceans* **117**, 1–18 (2012).
- Balaguer, J., Koch, F., Hassler, C. & Trimbom, S. Iron and manganese co-limit the growth of two phytoplankton groups dominant at two locations of the Drake Passage. *Commun. Biol.* **5**, 207 (2022).
- MacGilchrist, G. A. et al. Reframing the carbon cycle of the subpolar Southern Ocean. *Sci. Adv.* **5**, 1–9 (2019).
- Dunne, J. P., Sarmiento, J. L. & Gnanadesikan, A. A synthesis of global particle export from the surface ocean and cycling through the ocean interior and on the seafloor. *Glob. Biogeochem. Cycles* **21**, 1–16 (2007).
- Moore, C. M. et al. Processes and patterns of oceanic nutrient limitation. *Nat. Geosci.* **6**, 701–710 (2013).
- Tagliabue, A. et al. The integral role of iron in ocean biogeochemistry. *Nature* **543**, 51–59 (2017).
- Browning, T. J. & Moore, C. M. Global analysis of ocean phytoplankton nutrient limitation reveals high prevalence of co-limitation. *Nat. Commun.* **14**, 1–12 (2023).
- Browning, T. J., Achterberg, E. P., Engel, A. & Mawji, E. Manganese co-limitation of phytoplankton growth and major nutrient drawdown in the Southern Ocean. *Nat. Commun.* **12**, 884 (2021).
- Hawco, N. J., Tagliabue, A. & Twining, B. S. Manganese limitation of phytoplankton physiology and productivity in the Southern Ocean. *Glob. Biogeochem. Cycles* **36**, e2022GB007382 (2022).
- Wyatt, N. J. et al. Phytoplankton responses to dust addition in the Fe–Mn co-limited eastern Pacific sub-Antarctic differ by source region. *Proc. Natl Acad. Sci. USA* **120**, 2017 (2023).
- Hayes, C. T. et al. Replacement times of a spectrum of elements in the North Atlantic based on thorium supply. *Glob. Biogeochem. Cycles* **32**, 1294–1311 (2018).
- van Hulst, M. et al. Manganese in the west Atlantic Ocean in the context of the first global ocean circulation model of manganese. *Biogeochemistry* **14**, 1123–1152 (2017).
- Pollard, R., Sanders, R., Lucas, M. & Statham, P. The Crozet natural iron bloom and export experiment (CROZEX). *Deep Sea Res. Part II Top. Stud. Oceanogr.* **54**, 1905–1914 (2007).
- Moore, C. M. et al. Iron-light interactions during the CROZEX natural iron bloom and EXport experiment (CROZEX) I: Phytoplankton growth and photophysiology. *Deep Sea Res. Part II Top. Stud. Oceanogr.* **54**, 2045–2065 (2007).
- McGillcuddy, D. J. et al. Iron supply and demand in an Antarctic shelf ecosystem. *Geophys. Res. Lett.* **42**, 8088–8097 (2015).



16. Middag, R., de Baar, H. J. W., Laan, P., Cai, P. H. & van Ooijen, J. C. Dissolved manganese in the Atlantic sector of the Southern Ocean. *Deep Sea Res. Part II Top. Stud. Oceanogr.* **58**, 2661–2677 (2011).
17. Gerringa, L. J. A. et al. Sources of iron in the Ross Sea Polynya in early summer. *Mar. Chem.* **177**, 447–459 (2015).
18. Sholkovitz, E. R., Sedwick, P. N. & Church, T. M. Influence of anthropogenic combustion emissions on the deposition of soluble aerosol iron to the ocean: empirical estimates for island sites in the North Atlantic. *Geochim. Cosmochim. Acta* **73**, 3981–4003 (2009).
19. Mahowald, N. M. et al. Atmospheric iron deposition: global distribution, variability, and human perturbations. *Ann. Rev. Mar. Sci.* **1**, 245–278 (2009).
20. Findlay, A. J. et al. Iron and sulfide nanoparticle formation and transport in nascent hydrothermal vent plumes. *Nat. Commun.* **10**, 1597 (2019).
21. Tagliabue, A. & Resing, J. Impact of hydrothermalism on the ocean iron cycle. *Philos. Trans. R. Soc. A Math. Phys. Eng. Sci.* **374**, 20150291 (2016).
22. German, C. R., Campbell, A. C. & Edmond, J. M. Hydrothermal scavenging at the Mid-Atlantic Ridge: modification of trace element dissolved fluxes. *Earth Planet. Sci. Lett.* **107**, 101–114 (1991).
23. Resing, J. A. et al. Basin-scale transport of hydrothermal dissolved metals across the South Pacific Ocean. *Nature* **523**, 200–203 (2015).
24. Fitzsimmons, J. N., Boyle, E. A. & Jenkins, W. J. Distal transport of dissolved hydrothermal iron in the deep South Pacific Ocean. *Proc. Natl Acad. Sci. USA* **111**, 16654–16661 (2014).
25. Wu, J., Wells, M. L. & Rember, R. Dissolved iron anomaly in the deep tropical–subtropical Pacific: evidence for long-range transport of hydrothermal iron. *Geochim. Cosmochim. Acta* **75**, 460–468 (2011).
26. Tagliabue, A. et al. Hydrothermal contribution to the oceanic dissolved iron inventory. *Nat. Geosci.* **3**, 252–256 (2010).
27. Yücel, M., Gartman, A., Chan, C. S. & Luther, G. W. Hydrothermal vents as a kinetically stable source of iron-sulphide-bearing nanoparticles to the ocean. *Nat. Geosci.* **4**, 367–371 (2011).
28. Findlay, A. J., Gartman, A., Shaw, T. J. & Luther, G. W. Trace metal concentration and partitioning in the first 1.5 m of hydrothermal vent plumes along the Mid-Atlantic Ridge: TAG, Snakepit, and Rainbow. *Chem. Geol.* **412**, 117–131 (2015).
29. Lough, A. J. M. et al. Soluble iron conservation and colloidal iron dynamics in a hydrothermal plume. *Chem. Geol.* **511**, 225–237 (2019).
30. Sander, S. G. & Koschinsky, A. Metal flux from hydrothermal vents increased by organic complexation. *Nat. Geosci.* **4**, 145–150 (2011).
31. Toner, B. M. et al. Preservation of iron(II) by carbon-rich matrices in a hydrothermal plume. *Nat. Geosci.* **2**, 197–201 (2009).
32. Lupton, J. Hydrothermal helium plumes in the Pacific Ocean. *J. Geophys. Res. Ocean.* **103**, 15853–15868 (1998).
33. Winckler, G., Newton, R., Schlosser, P. & Crone, T. J. Mantle helium reveals Southern Ocean hydrothermal venting. *Geophys. Res. Lett.* **37**, 1–5 (2010).
34. Toggweiler, J. R. & Samuels, B. On the ocean's large-scale circulation near the limit of no vertical mixing. *J. Phys. Oceanogr.* **28**, 1832–1852 (1998).
35. Tagliabue, A. et al. Surface-water iron supplies in the Southern Ocean sustained by deep winter mixing. *Nat. Geosci.* **7**, 314–320 (2014).
36. Schine, C. et al. Massive bloom fed by elevated iron of possible hydrothermal origin in the Pacific Sector of the Southern Ocean. In *Ocean Science Meeting CT23A-03* <https://doi.org/10.1038/s41467-021-21339-5> (2020).
37. Ardyna, M. et al. Hydrothermal vents trigger massive phytoplankton blooms in the Southern Ocean. *Nat. Commun.* **10**, 1–8 (2019).
38. Bonnet, S. et al. Natural iron fertilization by shallow hydrothermal sources fuels diazotroph blooms in the ocean. *Science* **380**, 812–817 (2023).
39. Tagliabue, A. et al. Constraining the contribution of hydrothermal iron to Southern Ocean export production using deep ocean iron observations. *Front. Mar. Sci.* **9**, 1–10 (2022).
40. Roshan, S., DeVries, T., Wu, J., John, S. & Weber, T. Reversible scavenging traps hydrothermal iron in the deep ocean. *Earth Planet. Sci. Lett.* **542**, 116297 (2020).
41. Kipp, L. E. et al. Radium isotopes as tracers of hydrothermal inputs and neutrally buoyant plume dynamics in the deep ocean. *Mar. Chem.* **201**, 51–65 (2018).
42. DeVries, T. & Holzer, M. Radiocarbon and helium isotope constraints on deep ocean ventilation and mantle-<sup>3</sup>He sources. *J. Geophys. Res. Oceans* **124**, 3036–3057 (2019).
43. Tamsitt, V. et al. Spiraling pathways of global deep waters to the surface of the Southern Ocean. *Nat. Commun.* **8**, 1–10 (2017).
44. Drake, H. F. et al. Lagrangian timescales of Southern Ocean upwelling in a hierarchy of model resolutions. *Geophys. Res. Lett.* **45**, 891–898 (2018).
45. Jenkins, W. J. Using excess <sup>3</sup>He to estimate Southern Ocean upwelling time scales. *Geophys. Res. Lett.* **47**, 1–10 (2020).
46. de Baar, H. J. W. et al. Low dissolved Fe and the absence of diatom blooms in remote Pacific waters of the Southern Ocean. *Mar. Chem.* **66**, 1–34 (1999).
47. Gourain, A. et al. Inputs and processes affecting the distribution of particulate iron in the North Atlantic along the GEOVIDE (GEOTRACES GA01) section. *Biogeosciences* **16**, 1563–1582 (2019).
48. Zheng, L., Minami, T., Takano, S. & Sohrin, Y. Distributions of aluminum, manganese, cobalt, and lead in the western South Pacific: interplay between the South and North Pacific. *Geochim. Cosmochim. Acta* **338**, 105–120 (2022).
49. Jenkins, W. J. et al. A comprehensive global oceanic dataset of helium isotope and tritium measurements. *Earth Syst. Sci. Data* **11**, 441–454 (2019).
50. Gamo, T. et al. Chemical characteristics of hydrothermal fluids from the TAG Mound of the Mid-Atlantic Ridge in August 1994: implications for spatial and temporal variability of hydrothermal activity. *Geophys. Res. Lett.* **23**, 3483–3486 (1996).
51. Fitzsimmons, J. N. et al. Iron persistence in a distal hydrothermal plume supported by dissolved–particulate exchange. *Nat. Geosci.* **10**, 195–201 (2017).
52. Carazzo, G., Jellinek, A. M. & Turchyn, A. V. The remarkable longevity of submarine plumes: implications for the hydrothermal input of iron to the deep-ocean. *Earth Planet. Sci. Lett.* **382**, 66–76 (2013).
53. Tagliabue, A. et al. The interplay between regeneration and scavenging fluxes drives ocean iron cycling. *Nat. Commun.* **10**, 1–8 (2019).
54. Well, R., Roether, W. & Stevens, D. P. An additional deep-water mass in Drake Passage as revealed by <sup>3</sup>He data. *Deep Sea Res. Part I Oceanogr. Res. Pap.* **50**, 1079–1098 (2003).
55. Reid, J. L. On the total geostrophic circulation of the South Pacific Ocean: flow patterns, tracers and transports. *Prog. Oceanogr.* **16**, 1–61 (1986).
56. Shaffer, G., Salinas, S., Pizarro, O., Vega, A. & Hormazabal, S. Currents in the deep ocean off Chile (30°S). *Deep Sea Res. Part I Oceanogr. Res. Pap.* **42**, 425–436 (1995).
57. Baker, E. T. & Massoth, G. J. Characteristics of hydrothermal plumes from two vent fields on the Juan de Fuca Ridge, northeast Pacific Ocean. *Earth Planet. Sci. Lett.* **85**, 59–73 (1987).
58. Klinkhammer, G., Rona, P., Greaves, M. & Elderfield, H. Hydrothermal manganese plumes in the Mid-Atlantic Ridge rift valley. *Nature* **314**, 727–731 (1985).
59. Lupton, J. E. & Craig, H. A major helium-3 source at 15°S on the east Pacific rise. *Science* **214**, 13–18 (1981).
60. Delandmeter, P. & Van Sebille, E. The Parcels v2.0 Lagrangian framework: new field interpolation schemes. *Geosci. Model Dev.* **12**, 3571–3584 (2019).
61. Maded, G. & Team, N. *NEMO ocean engine*. [https://epic.awi.de/id/eprint/39698/1/NEMO\\_book\\_v6039.pdf](https://epic.awi.de/id/eprint/39698/1/NEMO_book_v6039.pdf) (2015).
62. Strub, P. T., James, C., Montecino, V., Rutllant, J. A. & Blanco, J. L. Ocean circulation along the southern Chile transition region

- (38°–46°S): mean, seasonal and interannual variability, with a focus on 2014–2016. *Prog. Oceanogr.* **172**, 159–198 (2019).
63. Forget, G. et al. ECCO version 4: an integrated framework for non-linear inverse modeling and global ocean state estimation. *Geosci. Model Dev.* **8**, 3071–3104 (2015).
64. Fukumori, I. & ECCO Consortium et al. ECCO Central Estimate (Version 4 Release 4). <https://www.ecco-group.org/products-ECCO-V4r4.htm> (2021).
65. Faure, V. & Speer, K. Deep circulation in the eastern South Pacific Ocean. *J. Mar. Res.* **70**, 748–778 (2012).
66. Beaulieu, S. E., Baker, E. T. & German, C. R. Where are the undiscovered hydrothermal vents on oceanic spreading ridges? *Deep Sea Res. Part II Top. Stud. Oceanogr.* **121**, 202–212 (2015).
67. Boström, K., Peterson, M. N. A., Joensuu, O. & Fisher, D. E. Aluminum-poor ferromanganous sediments on active oceanic ridges. *J. Geophys. Res.* **74**, 3261–3270 (1969).
68. Baker, E. T. et al. How many vent fields? New estimates of vent field populations on ocean ridges from precise mapping of hydrothermal discharge locations. *Earth Planet. Sci. Lett.* **449**, 186–196 (2016).
69. Buongiorno Nardelli, B. et al. Southern Ocean mixed-layer seasonal and interannual variations from combined satellite and in situ data. *J. Geophys. Res. Ocean.* **122**, 10042–10060 (2017).
70. Bachman, S. D. & Klocker, A. Interaction of jets and submesoscale dynamics leads to rapid ocean ventilation. *J. Phys. Oceanogr.* **50**, 2873–2883 (2020).
71. Cutter, G. A. et al. Sampling and sample-handling protocols for GEOTRACES cruises, [Other] (GEOTRACES, 2010) <https://doi.org/10.10013/epic.42722.d001>.
72. Birchill, A. J. et al. Seasonal iron depletion in temperate shelf seas. *Geophys. Res. Lett.* **44**, 8987–8996 (2017).
73. Floor, G. H. et al. Combined uncertainty estimation for the determination of the dissolved iron amount content in seawater using flow injection with chemiluminescence detection. *Limnol. Oceanogr. Methods* **13**, 673–686 (2015).
74. Worsfold, P. J. et al. Estimating uncertainties in oceanographic trace element measurements. *Front. Mar. Sci.* **6**, 1–9 (2019).
75. Grasshoff, K., Kremling, K. & Ehrhardt, M. *Methods of Seawater Analysis* (Wiley, 1999) <https://doi.org/10.1002/9783527613984>.
76. Bouillon, S., Morales Maqueda, M. Á., Legat, V. & Fichfet, T. An elastic-viscous-plastic sea ice model formulated on Arakawa B and C grids. *Ocean Model.* **27**, 174–184 (2009).
77. Brodeau, L., Barnier, B., Treguier, A. M., Penduff, T. & Gulev, S. An ERA40-based atmospheric forcing for global ocean circulation models. *Ocean Model.* **31**, 88–104 (2010).
78. van Sebille, E. et al. Lagrangian ocean analysis: fundamentals and practices. *Ocean Model.* **121**, 49–75 (2018).
79. Baker, C. A., Martin, A. P., Yool, A. & Popova, E. Biological carbon pump sequestration efficiency in the North Atlantic: a leaky or a long-term sink? *Glob. Biogeochem. Cycles* <https://doi.org/10.1029/2021gb007286> (2022).
80. German, C. R. et al. Diverse styles of submarine venting on the ultraslow spreading Mid-Cayman Rise. *Proc. Natl Acad. Sci. USA* **107**, 14020–14025 (2010).
81. Baker, E. T. et al. Hydrothermal venting in magma deserts: the ultraslow-spreading Gakkel and Southwest Indian Ridges. *Geochem. Geophys. Geosyst.* **5**, 1–29 (2004).
82. Beaulieu, S. E., Baker, E. T., German, C. R. & Maffei, A. An authoritative global database for active submarine hydrothermal vent fields. *Geochem. Geophys. Geosyst.* **14**, 4892–4905 (2013).
83. Kawabe, M. & Fujio, S. Pacific Ocean circulation based on observation. *J. Oceanogr.* **66**, 389–403 (2010).

## Acknowledgements

A.J.B., C.A.B., N.J.W., K.P., H.J.V., A.M., S.J.U., C.M.M., S.O. and A.P.M. were supported by the Natural Environment Research Council (NERC) funding for the CUSTARD project (NE/P021247/2; NE/P021336/1; NE/P021328/1). I.T. was supported by the ARIES DTP (NE/V009877/1). We would like to thank the NMF technicians and the RRS Discovery ship's captain, officers crew for their support during DY111. We would like to acknowledge and thank the parcels (<https://oceanparcels.org/>) developers, the JASMIN service (<https://jasmin.ac.uk/>), the ECCO Consortium and Ocean Data View developers (<https://odv.awi.de>) for their efforts. We would like to thank Alessandro Tagliabue and William Jenkins for their useful and informative discussions around our research.

## Author contributions

A.J.B. and C.A.B. wrote the initial draft and all co-authors contributed to draft revisions. A.J.B., C.A.B., N.J.W., K.P., H.J.V., C.M.M., I.T., A.M., S.J.U. and A.P.M. participated in the field campaign. A.J.B. and N.J.W. conducted trace metal (micronutrient) analysis. K.P. performed macronutrient analysis. H.J.V. processed conductivity-temperature-depth sensor package datasets. C.A.B. performed Lagrangian modelling experiments and analysis. S.O. carried out the water mass analysis. A.P.M., C.M.M., S.J.U. and A.M. wrote and planned the original research questions and funding proposal. A.P.M. led the research programme. The views expressed in this paper are those of the authors alone, and not the organisations for which they work.

## Competing interests

The authors declare no competing interests.

## Additional information

**Supplementary information** The online version contains supplementary material available at <https://doi.org/10.1038/s43247-024-01564-8>.

**Correspondence** and requests for materials should be addressed to Antony J. Birchill or Chelsey A. Baker.

**Peer review information** *Communications Earth & Environment* thanks John Dunne, Jessica Fitzsimmons and the other, anonymous, reviewer(s) for their contribution to the peer review of this work. Primary Handling Editors: Annie Bourbonnais, Heike Langenberg and Alienor Lavergne. A peer review file is available.

**Reprints and permissions information** is available at <http://www.nature.com/reprints>

**Publisher's note** Springer Nature remains neutral with regard to jurisdictional claims in published maps and institutional affiliations.

**Open Access** This article is licensed under a Creative Commons Attribution 4.0 International License, which permits use, sharing, adaptation, distribution and reproduction in any medium or format, as long as you give appropriate credit to the original author(s) and the source, provide a link to the Creative Commons licence, and indicate if changes were made. The images or other third party material in this article are included in the article's Creative Commons licence, unless indicated otherwise in a credit line to the material. If material is not included in the article's Creative Commons licence and your intended use is not permitted by statutory regulation or exceeds the permitted use, you will need to obtain permission directly from the copyright holder. To view a copy of this licence, visit <http://creativecommons.org/licenses/by/4.0/>.

© Crown 2024